

## Article

# Prediction Model of Shrinkage Crack Propagation in Cross-Section of Timber Components

Panpan Tian <sup>1,\*</sup>, Hongxing Qiu <sup>2</sup>, Jianhong Han <sup>3,\*</sup>, Hongmin Li <sup>4</sup> and Xia Han <sup>1</sup>

<sup>1</sup> School of Civil Engineering and Architecture, Xinjiang University, Urumqi 830047, China; hanxiaixa@xju.edu.cn

<sup>2</sup> Key Laboratory of Concrete and Prestressed Concrete Structures of Ministry of Education, School of Civil Engineering, Southeast University, Nanjing 211189, China; 101000854@seu.edu.cn

<sup>3</sup> School of Civil Engineering, Xinjiang Institute of Engineering, Urumqi 830023, China

<sup>4</sup> College of Materials Science and Engineering, Nanjing Forestry University, Nanjing 210037, China; lihongmin@njfu.edu.cn

\* Correspondence: tianpanpan@xju.edu.cn (P.T.); 2021200@xjue.edu.cn (J.H.)

**Abstract:** Shrinkage cracks severely affect the safety of wood structures. Therefore, the moisture stress distribution of shrinkage cracks should be analyzed, and the interface crack depth of wood components predicted. In this paper, the equilibrium conditions, physical conditions, geometric conditions, and coordination equations of the disk humidity stress under a moisture content gradient  $\Delta w$  are deduced by referring to the elastic analytical solution model of temperature stress. Moreover, the humidity stress distribution equation is established, which is verified via the finite element method. The critical water content and shrinkage crack depth prediction models are further deduced based on the humidity stress distribution. The usability of the model is further verified using the test data of actual engineered wood components. The results demonstrate that the moisture stress is not determined by the initial moisture content  $W_i$ , equilibrium moisture content  $W_e$ , or member size but by moisture content gradient  $\Delta w$ . The shrinkage crack prediction model of wood components in cross-section can be applied to actual engineering prediction to provide a theoretical basis for the reinforcement measures and safety evaluation of wood structures.

**Keywords:** wood components; moisture content gradient; humidity stress distribution; shrinkage crack depth; detection



**Citation:** Tian, P.; Qiu, H.; Han, J.; Li, H.; Han, X. Prediction Model of Shrinkage Crack Propagation in Cross-Section of Timber Components. *Buildings* **2023**, *13*, 2505. <https://doi.org/10.3390/buildings13102505>

Academic Editor: Thomas Tannert

Received: 23 August 2023

Revised: 14 September 2023

Accepted: 27 September 2023

Published: 2 October 2023



**Copyright:** © 2023 by the authors. Licensee MDPI, Basel, Switzerland. This article is an open access article distributed under the terms and conditions of the Creative Commons Attribution (CC BY) license (<https://creativecommons.org/licenses/by/4.0/>).

## 1. Introduction

Timber is a biopolymeric, hygroscopic, and anisotropic composite material. Shrinkage cracks are commonly observed in wood buildings, as shown in Figure 1. The crack depth in cross-section can significantly affect the durability of timber components. Generally, the generation and expansion of shrinkage cracks involve the following three steps, as illustrated in Figure 2: a moisture content gradient  $\Delta w$  caused by environmental change, humidity stress distribution caused by uneven dimensional changes in different directions, and shrinkage cracks.

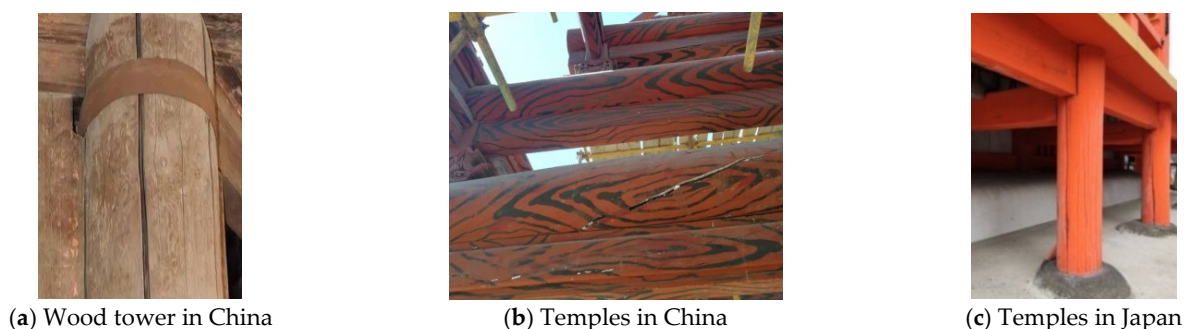
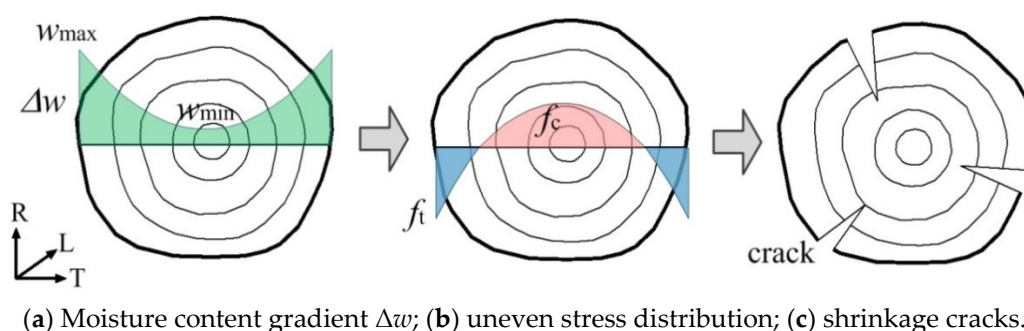


Figure 1. Shrinkage cracks of wood buildings.



(a) Moisture content gradient  $\Delta w$ ; (b) uneven stress distribution; (c) shrinkage cracks.

Figure 2. Generation steps of shrinkage cracks.

Generally, the humidity stress distribution is critical for the further analysis of shrinkage cracks. So far, wood shrinkage experiments for testing the humidity stress distribution have garnered much attention. Kang [1] applied the ring slice method to study the relationship between the radial moisture content distribution and chordwise strain of a tree disc under high-frequency vacuum drying and concluded that cracking is mainly related to the radial distribution of moisture content. Svensson [2] measured the radial humidity stress distribution of Norway spruce under different moisture contents and concluded that the humidity stress inside the wooden component is highly correlated with the relative humidity history, and the change in humidity generates larger humidity stress inside the component. Jönsson [3–5], similar to Svensson, conducted a sample test and measured the humidity stress inside each sample via a nondestructive testing method and cut strip release method. The results demonstrated that a change in relative humidity leads to a change in the humidity stress on the outer surface of the wood from 0.66 MPa to 0.34 MPa, whereas the change in the internal humidity stress varies from  $-0.11$  MPa to 0.85 MPa. Moreover, the maximum humidity tensile stress exceeds the transverse grain tensile strength of the wood. Gereke [6] studied the humidity stress in a cross-laminated timber (CLT) wood board via the cutting strip release method and finite element simulation and found that the material of the CLT intermediate layer has a significant effect on its internal humidity stress. Fragiacomio [7] studied the influence of different types of environments on the internal humidity stress of the components. The results demonstrated that the change in relative humidity in the natural environment can cause high-humidity stresses inside components, even exceeding the transverse grain tensile strength of wood, resulting in cracking. After studying the surface hardening and residual deformation of beech during drying, Morihiko [8] found the surface and inner layers of wood to be under tensile and compression deformation at the beginning of drying, respectively. Mohager [9] conducted long-term loading tests on glulam beams processed from pine under cyclic changes in external relative humidity (15–90%). Notably, the change in humidity has an influence on the deformation recovery after unloading. Cheng [10] studied the changes in internal moisture content, strain, and stress during wood curing. During the curing period, the wood was placed in

the constant temperature and humidity test environment box, with the temperature and humidity setting of 65 °C and 70%, respectively. The results demonstrated that wood curing treatment reduces the difference between moisture content and internal stress in wood. Gao [11] studied the stress distribution through humidity cycling experiments on larch and sylvestris. Arends [12] studied the effect of asymmetric moisture distribution on the change in board stress. Moreover, the author designed experiments to derive the moisture diffusion coefficient and linear hygroscopic expansion coefficient of wood to analyze the stress induced by the exposure of one side of the oak board to moisture. Liu [13] studied the effect of relative humidity on the shrinkage stress in elm wood during drying. The results demonstrated that the shrinkage stress gradually increases during drying and tends to stabilize after peaking.

However, theoretical analyses of the humidity stress distribution in the cross-sections of timber components remain scarce. Wang [14] investigated the relationship between drying stress and cracks from a microscopic perspective and found that wood is prone to stress concentration during drying. When the drying stress exceeds the tensile strength of the wood, the wood will crack. Kawa [15] described the rheological properties of wood through a viscoelastic anisotropic stress–strain relationship and established a stress function with free shrinkage, actual shrinkage, and inelastic strain as parameters. Chen [16] applied the Luikov heat and mass transfer model to perform finite element analysis on the temperature and humidity stress of the horizontal grain caused by cyclic changes in ambient temperature and humidity in glulam straight and curved beams. The calculation revealed that the glulam beams are subject to additional stresses due to changes in ambient temperature and humidity, the maximum stress of temperature stress is 0.016 MPa, and the humidity stress can reach 2.6 MPa. Gereke [17] applied a three-dimensional material model considering elastic deformation, moisture-induced expansion, and mechanical adsorption creep to study the effect of material parameters on the numerical simulation results. They further analyzed the stress caused by changes in water content. Angst [18] numerically simulated the distribution and development of moisture-induced stress in the cross-section of glulam during the moisture absorption process and found that the local stress was significantly greater than the average stress. Gao [11] established a finite element model based on the wood humidity cycle test and deduced a formula for calculating the temperature and humidity stress of the wood, and the results of the two were in good agreement. Arends [19] utilized the diffusion equation and linear elasticity theory to analyze the stress distribution caused by a single-side exposure of an oak board to moisture.

More recently, researchers have started to pay attention to the contribution of wood shrinkage cracking. Zhao [20] dried a 30 mm thick birch tray at a constant temperature of 40 °C and 60 °C and gradually decreasing relative humidity. The author also studied its drying characteristics (drying curve and rate, drying curve and moisture content gradient of heartwood and sapwood, and water content and strain distribution along the radial direction) and drying cracking characteristics (generation period, location, morphology). The research demonstrated that the roundness and cross-sectional area of the tree disc are the main factors affecting the total crack length and the average crack width. Fan [21] conducted a tracking test of the air-drying process in larch and evaluated the changes in wood moisture content and shrinkage cracks with time. Ample statistics on the position, shape, and depth of shrinkage cracks in the components were generated, and a large amount of test data were accumulated. Based on the experimental data of Fan, Wang [22] obtained the variation law of the relative depth of lateral shrinkage cracks with water content. Angellier [23] conducted creep fracture tests on small specimens of double cantilever beams made of Douglas fir and white fir. Initial cracks with an initial length of 50 mm were set at the left end of each 700 mm long specimen, and they were placed in an environment where the temperature was 25 °C, whereas the relative humidity was periodically changed between 40% and 90%. The relationship between the crack length, moisture content of the specimen, and time during the test was established. The results demonstrated that the starting point of crack propagation occurred in the dehumidification stage. The white fir

broke almost completely after three drying and wetting cycles, whereas the Douglas fir was not completely destroyed after more than four cycles. Chen [24] studied moisture transfer and the formation and propagation of cross-section shrinkage cracks in six cylindrical Anhui fir trees in a dry environment. Different specimens with cracks at the same position had almost the same crack growth rate, although the crack initiation time was different.

The aforementioned literature reveals that the humidity stress distribution and prediction of shrinkage crack are very complicated. Although the research results collected by some scholars are extensive, the following shortcomings persist. (1) Notably, most of the abovementioned studies treated the influencing factors of humidity stress. However, cross-sectional theoretical analytical models or even related approximate models are almost nonexistent. (2) Generally, the crack depth of wood components is roughly predicted by testing actual engineering components. However, a model for predicting crack depth according to environmental and material factors has yet to be established. (3) Some inaccurate shrinkage crack depth prediction models have not been verified using tests or actual engineering tracking data.

Considering the prediction of shrinkage cracks in cross-section and the above gaps, this article is structured as follows: In Section 2, an accurate humidity stress distribution analytical solution is derived in detail and verified via ABAQUS. Simultaneously, the prediction expressions of critical moisture content gradient and dry shrinkage crack depth are proposed in Section 3. The shrinkage crack depth prediction model is supported by practical wood component detection in Section 4. Finally, conclusions from this study are highlighted in Section 5.

## 2. Humidity Stress Distribution

An accurate humidity stress distribution expression analysis is a prerequisite for an efficient prediction model of shrinkage crack propagation in cross-section—specifically, an analytical solution.

### 2.1. Analytical Solution of Stress Distribution

Assuming that the water content drops uniformly by  $\Delta w$ , the cross-section shrinks uniformly from the dotted line to the solid line, as shown in Figure 3. The sector block with the included angle  $\theta$ , outer side of the section  $\delta_R(R) = R\alpha_R\Delta w$ , corresponding deformation value of the hoop during radial contraction (the difference between the dashed line and the solid line in the sector range)  $\delta'_T(R) = R\theta - (R - \delta_R)\theta = \delta R\theta = R\theta\alpha_R\Delta w$ , and tangential contraction value  $\delta_T(R) = R\theta\alpha_T\Delta w$  are considered.

The radial compressive stress in the surrounding material should be 0 ( $\rho = R$ ). The smaller the  $\rho$  value is, the larger the compressive stress value (stress increment  $d\sigma_R > 0$ ) and compressive deformation value. Moreover, radial compression deformation reduces the difference between the total radial deformation (shrinkage deformation and stress deformation) and the tangential shrinkage deformation, thus reducing the tangential tensile stress. When  $\rho < \rho_0$ , the radial compressive stress increment  $d\sigma_R < 0$ , and the tangential tensile stress transforms into compressive stress. The compressive stress always acts in the radial direction, and its value gradually increases from 0 on the outside.

At the position  $\rho = \rho_0$ , the circumferential shrinkage deformation is equal to the sum of the radial shrinkage deformation and the compression deformation. When  $\rho < \rho_0$ , the sum of the radial shrinkage deformation and the compression deformation is greater than the tangential shrinkage deformation, and the tangential direction must have compression deformation to meet the deformation coordination condition.

Taking the microelement as an example (as shown in Figure 3c), the equilibrium differential equation and the deformation coordination equation should be established and the physical conditions (stress–strain relationship and dry shrinkage–moisture content relationship, both of which are linear relationships) applied. Notably, the radial shrinkage deformation at the  $\rho$  position can be expressed as  $\delta_R(\rho) = \rho\alpha_R\Delta w$  (in the case of uniform water content distribution), but the compression deformation needs to be integrated from 0

to  $R$ . The tangential direction is uniform due to axial symmetry, regardless of whether the deformation is shrinkage or stretching. When  $\alpha_R = \alpha_T$ , the uniform shrinkage meets the deformation coordination condition, and no tangential tensile stress occurs. Because  $\alpha_T > \alpha_R$ , the tangential shrinkage deformation is greater than the uniform shrinkage deformation, and tensile deformation must be present to meet the deformation coordination condition.

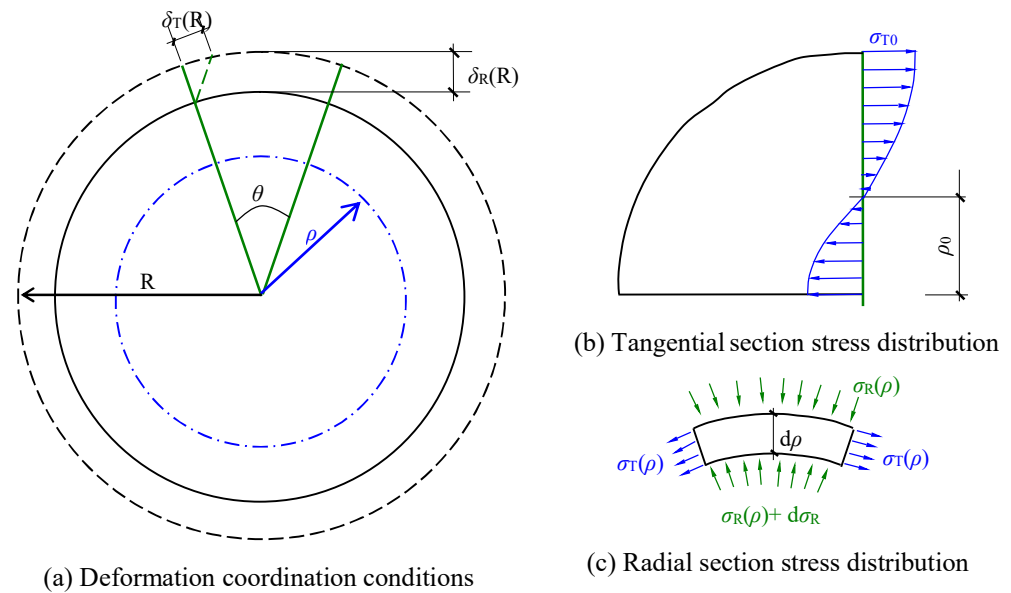


**Figure 3.** Stress analysis of wood before cracking.

### 2.1.1. Balance Condition

The radial force balance condition (pull is positive) is established according to the force analysis of the microelement body in Figure 3c, as given in Equation (1).

$$\frac{d\sigma_R}{d\rho} = \frac{\sigma_T - \sigma_R}{\rho}, \quad \sigma_T = \rho \frac{d\sigma_R}{d\rho} + \sigma_R \quad (1)$$

### 2.1.2. Constitutional Relationship

The force strain in the radial and circumferential directions in orthotropic materials is shown in Equation (2).

$$\begin{cases} \varepsilon_R = \frac{\sigma_R - \nu_{RT}\sigma_T}{E_R} = \frac{\sigma_R}{E_R} - \frac{\nu_{RT}}{E_R} \left[ \rho \frac{d\sigma_R}{d\rho} + \sigma_R \right] \Rightarrow \varepsilon_R = \frac{(1-\nu_{RT})\sigma_R}{E_R} - \frac{\nu_{RT}}{E_R} \rho \frac{d\sigma_R}{d\rho} \\ \varepsilon_T = \frac{\sigma_T - \nu_{TR}\sigma_R}{E_T} = \frac{\rho}{E_T} \frac{d\sigma_R}{d\rho} + \frac{\sigma_R}{E_T} - \frac{\nu_{TR}\sigma_R}{E_T} \Rightarrow \varepsilon_T = \frac{\rho}{E_T} \frac{d\sigma_R}{d\rho} + \frac{\sigma_R(1-\nu_{TR})}{E_T} \end{cases} \quad (2)$$

The radial shrinkage deformation  $\delta_{R,sh}(\rho)$  and the radial force deformation are expressed by Equations (3) and (4).

$$\delta_{R,sh}(\rho) = \alpha_R \int_0^\rho \Delta w(t) dr = \rho \alpha_R \Delta w(t) \quad (3)$$

$$\begin{aligned} \delta_{R,F} &= \int_0^\rho \varepsilon_R(r) dr \\ \Rightarrow \delta_{R,F} &= \frac{(1-\nu_{RT})}{E_R} \int_0^\rho \sigma_R dr - \frac{\nu_{RT}}{E_R} \int_0^\rho r d\sigma_R \\ \Rightarrow \delta_{R,F} &= \frac{(1-\nu_{RT})}{E_R} \int_0^\rho \sigma_R dr - \frac{\nu_{RT}}{E_R} [\rho \sigma_R - \int_0^\rho \sigma_R dr] \\ \Rightarrow \delta_{R,F} &= \frac{1}{E_R} \int_0^\rho \sigma_R dr - \frac{\nu_{RT}\rho\sigma_R}{E_R} \end{aligned} \quad (4)$$

The tangential shrinkage deformation and the tangential force deformation are expressed by Equations (5) and (6).

$$\delta_{T,sh}(\rho) = \rho d\theta \alpha_T \Delta w(t) \quad (5)$$

$$\begin{aligned} \delta_{T,F}(\rho) &= \rho d\theta \varepsilon_T \\ \Rightarrow \delta_{T,F} &= \rho d\theta \left[ \frac{\rho}{E_T} \frac{d\sigma_R}{d\rho} + \frac{\sigma_R(1-\nu_{TR})}{E_T} \right] \\ \Rightarrow \delta_{T,F} &= d\theta \left[ \frac{\rho^2}{E_T} \frac{d\sigma_R}{d\rho} + \frac{\rho\sigma_R(1-\nu_{TR})}{E_T} \right] \end{aligned} \quad (6)$$

### 2.1.3. Geometric Condition

The displacement coordination conditions are shown in Equation (7).

$$\delta_T = d\theta \delta_R; \delta_{T,F}(\rho) + \delta_{T,sh}(\rho) = d\theta [\delta_{R,F}(\rho) + \delta_{R,sh}(\rho)] \quad (7)$$

### 2.1.4. Fundamental Equation

The displacement coordination condition is shown in Equation (8).

$$\begin{aligned} \frac{\rho^2}{E_T} \frac{d\sigma_R}{d\rho} + \frac{\rho\sigma_R(1-\nu_{TR})}{E_T} + \rho \alpha_T \Delta w(t) &= \frac{1}{E_R} \int_0^\rho \sigma_R dr - \frac{\nu_{RT}\rho\sigma_R}{E_R} + \rho \alpha_R \Delta w(t) \\ \rho^2 \frac{d\sigma_R}{d\rho} + (1-\nu_{TR})\rho\sigma_R + \alpha_E \nu_{RT}\rho\sigma_R - \alpha_E \int_0^\rho \sigma_R dr + \rho(\alpha_T - \alpha_R)E_T \Delta w(t) &= 0 \end{aligned} \quad (8)$$

$\rho$  obtained from the above formula is expressed in Equation (9).

$$\begin{aligned} \rho^2 \frac{d^2\sigma_R}{d\rho^2} + 2\rho \frac{d\sigma_R}{d\rho} + (1-\nu_{TR})\sigma_R + (1-\nu_{TR})\rho \frac{d\sigma_R}{d\rho} + \alpha_E \nu_{RT}\sigma_R \\ + \alpha_E \nu_{RT}\rho \frac{d\sigma_R}{d\rho} - \alpha_E \sigma_R + K = 0 \end{aligned} \quad (9)$$

The above formula is then simplified as Equation (10).

$$\rho^2 \frac{d^2\sigma_R}{d\rho^2} + 3\rho \frac{d\sigma_R}{d\rho} + \sigma_R(1-\alpha_E) + K = 0 \quad (10)$$

Among them,  $\alpha_E = E_T/E_R$ ,  $K = E_T(\alpha_T - \alpha_R)\Delta w(t)$ .

### 2.1.5. Boundary Conditions

Boundary condition 1 is given in Equation (11).

$$\int_0^R \sigma_T d\rho = 0, \quad \rho = R, \sigma_R = 0 \quad (11)$$

Boundary condition 2 is given in Equation (12).

$$\sigma_R(R) = 0 \quad (12)$$

### 2.1.6. Solution

Let  $\rho = e^t$ , then  $t = \ln\rho$ :

$$\frac{d\sigma_R}{d\rho} = \frac{1}{\rho} \frac{d\sigma_R}{dt}, \quad \frac{d^2\sigma_R}{d\rho^2} = \frac{1}{\rho^2} \frac{d^2\sigma_R}{dt^2} - \frac{1}{\rho^2} \frac{d\sigma_R}{dt} \quad (13)$$

The differential equation is transformed into Equation (14).

$$\frac{d^2\sigma_R}{dt^2} + 2\frac{d\sigma_R}{dt} + \sigma_R(1-\alpha_E) = -K \quad (14)$$

The characteristic equation and solution are expressed in Equation (15).

$$\begin{cases} r^2 + 2r + (1 - \alpha_E) = 0 \\ r_1 = -1 + \sqrt{\alpha_E} \\ r_2 = -1 - \sqrt{\alpha_E} \end{cases} \quad (15)$$

The general solution of the homogeneous equation is given in Equation (16).

$$\sigma_R = C_1 e^{r_1 t} + C_2 e^{r_2 t} = C_1 \rho^{r_1} + C_2 \rho^{r_2} \quad (16)$$

The special solutions are presented in Equation (17).

$$\begin{cases} \sigma_R = C_3 \\ C_3(1 - \alpha_E) = -K \end{cases} \Rightarrow C_3 = -\frac{K}{(1 - \alpha_E)} \quad (17)$$

The general solution is expressed in Equations (18)–(20).

$$\begin{cases} \sigma_R = C_1 \rho^{-(1-\sqrt{\alpha_E})} + C_2 \rho^{-(1+\sqrt{\alpha_E})} - \frac{K}{(1-\alpha_E)} \\ \sigma_T = \rho \frac{d\sigma_R}{d\rho} + \sigma_R \Rightarrow \sigma_T = C_1 \sqrt{\alpha_E} \rho^{-(1-\sqrt{\alpha_E})} - C_2 \sqrt{\alpha_E} \rho^{-(1+\sqrt{\alpha_E})} - \frac{K}{(1-\alpha_E)} \end{cases} \quad (18)$$

$$\int_0^R \sigma_T d\rho = 0 \Rightarrow C_2 = 0 \quad (19)$$

$$\sigma_R(R) = 0 \Rightarrow C_1 R^{-(1-\sqrt{\alpha_E})} - \frac{K}{(1-\alpha_E)} = 0 \Rightarrow C_1 = \frac{KR^{(1-\sqrt{\alpha_E})}}{(1-\alpha_E)} \quad (20)$$

The stress distribution in the disc under uniform moisture content is shown in Figure 3, and the stress distribution conforms to Equation (21).

$$\begin{cases} \sigma_R = -\frac{K}{1-\alpha_E} \left[ 1 - (\rho/R)^{(\sqrt{\alpha_E}-1)} \right] \\ \sigma_T = -\frac{K}{1-\alpha_E} \left[ 1 - \sqrt{\alpha_E} (\rho/R)^{(\sqrt{\alpha_E}-1)} \right] \end{cases} \quad (21)$$

The position where the tangential stress is equal to zero  $\rho_0$  is calculated as Equation (22).

$$\rho_0/R = \exp\left(\frac{0.5 \ln \alpha_E}{(1 - \sqrt{\alpha_E})}\right) \quad (22)$$

## 2.2. Numerical Simulation of Stress Distribution

ABAQUS 6.14, a finite element analysis software package, has a mature heat transfer function module. Because the heat transfer and humidity transfer of wood components are similar, the ABAQUS heat transfer module is used to analyze the humidity field of wood components. The key parameters and governing equations are presented in Tables 1 and 2.

**Table 1.** Parameters analogy of unsteady heat and moisture transfer.

Heat Transfer		Humidity Transfer	
Temperature	$T(K)$	Moisture content	$W$ (%)
Initial temperature	$T_i$	Initial moisture content	$W_i$
Ambient temperature	$T_e$	Equilibrium moisture content	$W_e$
Surface temperature of the object	$T_s$	Surface moisture content	$W_s$
Thermal conductivity	$\alpha$ (m <sup>2</sup> /s)	Water diffusion coefficient	$D$ (m <sup>2</sup> /s)
Surface heat exchange coefficient	$h$ (W/m <sup>2</sup> /K)	Surface humidity divergence coefficient	$S$ (m/s)

**Table 2.** Analogy of two-dimensional Fick's law governing equations for unsteady heat and moisture transfer.

Coordinates	Heat Transfer	Humidity Transfer
Cartesian coordinates	$\frac{\partial T}{\partial t} = \alpha \left( \frac{\partial^2 T}{\partial x^2} + \frac{\partial^2 T}{\partial y^2} + \frac{\partial^2 T}{\partial z^2} \right)$	$\frac{\partial W}{\partial t} = D \left( \frac{\partial^2 W}{\partial x^2} + \frac{\partial^2 W}{\partial y^2} + \frac{\partial^2 W}{\partial z^2} \right)$
Cylindrical coordinates	$\frac{1}{\alpha} \frac{\partial T}{\partial t} = \frac{1}{r} \frac{\partial}{\partial r} \left( r \frac{\partial T}{\partial r} \right) + \frac{\partial^2 T}{\partial z^2}$	$\frac{1}{D} \frac{\partial W}{\partial t} = \frac{1}{r} \frac{\partial}{\partial r} \left( r \frac{\partial W}{\partial r} \right) + \frac{\partial^2 W}{\partial z^2}$
Spherical coordinates	$\frac{1}{\alpha} \frac{\partial T}{\partial t} = \frac{1}{r^2} \frac{\partial}{\partial r} \left( r^2 \frac{\partial T}{\partial r} \right) + \frac{1}{r^2 \sin^2 \varphi} \left( \frac{\partial^2 T}{\partial \varphi^2} \right)$	$\frac{1}{D} \frac{\partial W}{\partial t} = \frac{1}{r^2} \frac{\partial}{\partial r} \left( r^2 \frac{\partial W}{\partial r} \right) + \frac{1}{r^2 \sin^2 \varphi} \left( \frac{\partial^2 W}{\partial \varphi^2} \right)$

To verify the correctness of the above analytical solution of the humidity stress, this section compares and analyzes the above models using ABAQUS. The finite element calculation is converted using the existing temperature field of the finite element analysis software, and the mesh size is approximately 2.5 mm. The finite element modeling method and material parameters comprise the authors' results. The main parameters and material parameters of the model are listed in Tables 3 and 4, respectively.

**Table 3.** Parameters of finite element models.

Group	Geometric Shape	Radius $\times$ Length $R \times L$ (mm)	$W_i$ (%)	$W_e$ (%)	Moisture Content Distribution Form	Restrictions
a	Disc	100 $\times$ 0	25	15	Uniform $\Delta w = 10\%$	Circle center
b	Disc	100 $\times$ 0	15	5	Uniform $\Delta w = 10\%$	Circle center
c	Disc	100 $\times$ 0	35	25	Uniform $\Delta w = 10\%$	Circle center
d	Disc	50 $\times$ 0	25	15	Uniform $\Delta w = 10\%$	Circle center
e	Disc	150 $\times$ 0	25	15	Uniform $\Delta w = 10\%$	Circle center
f	Disc	100 $\times$ 0	20	15	Uniform $\Delta w = 5\%$	Circle center
g	Disc	100 $\times$ 0	30	15	Uniform $\Delta w = 15\%$	Circle center
h	Cylinder	100 $\times$ 300	25	15	Uniform $\Delta w = 10\%$	Both ends of circle center
i	Cylinder	100 $\times$ 1000	25	15	Uniform $\Delta w = 10\%$	Both ends of circle center

**Table 4.** Parameters of material.

Directions	Elastic Modulus (MPa)	Compressive Strength (MPa)	Tensile Strength (MPa)	Shrinkage/Swelling Coefficient (%)
R	$E_R = 1048$ (16.1%)	$f_{c,R} = 3.07$ (12.23%)	$f_{t,R} = 3.07$ (12.23%)	$\alpha_R = 0.139$
T	$E_T = 594$ (22.7%)	$f_{c,T} = 2.67$ (13.44%)	$f_{t,T} = 2.67$ (13.44%)	$\alpha_T = 0.255$
L	$E_L = 12,888$ (6.9%)	$f_{c,L} = 36.25$ (10.43%)	$f_{t,L} = 36.25$ (10.43%)	$\alpha_L = 0.019$
Directions	Poisson ratio	Shear modulus (MPa)		
RT	$\nu_{RT} = 0.43$	$G_{RT} = 232$		
RL	$\nu_{RL} = 0.03$	$G_{RT} = 967$		
TL	$\nu_{TL} = 0.02$	$G_{RT} = 773$		

The typical finite element results from the above modeling method and material parameters are listed in Figures 4 and 5.

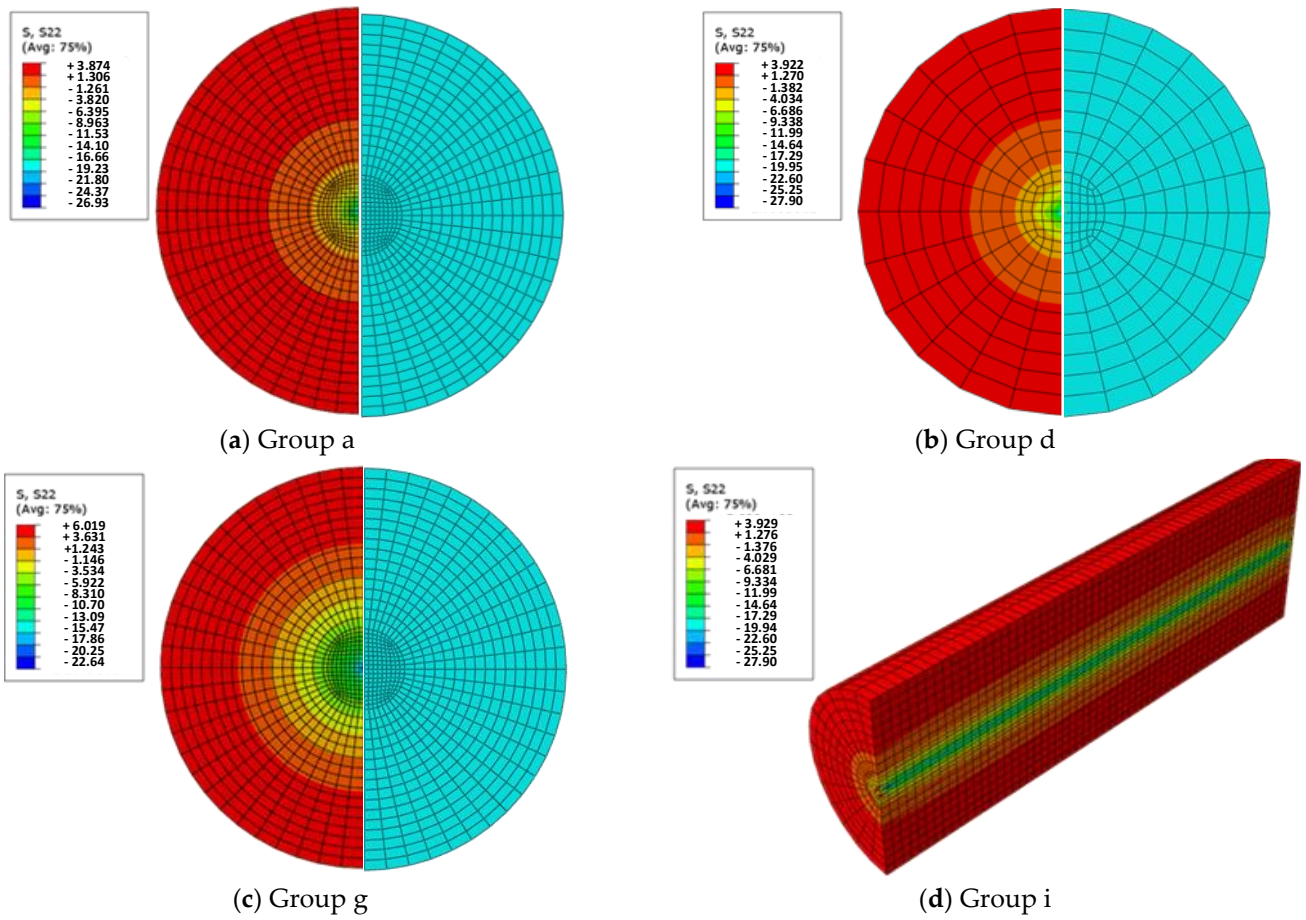
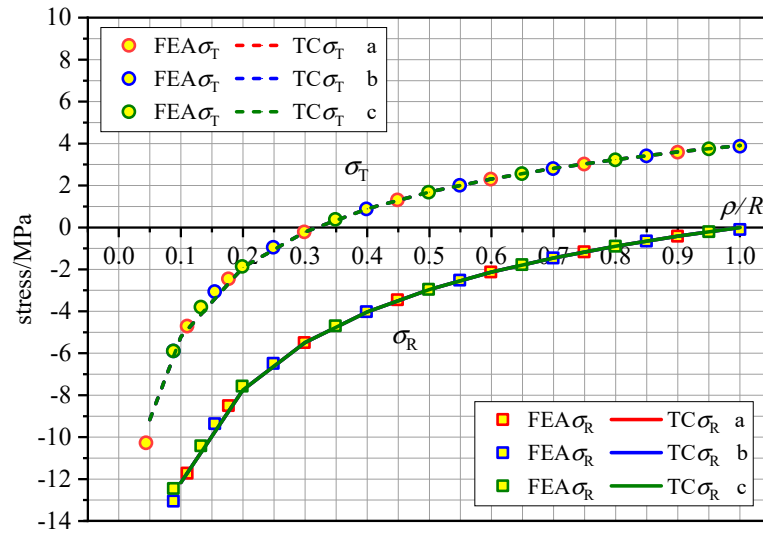
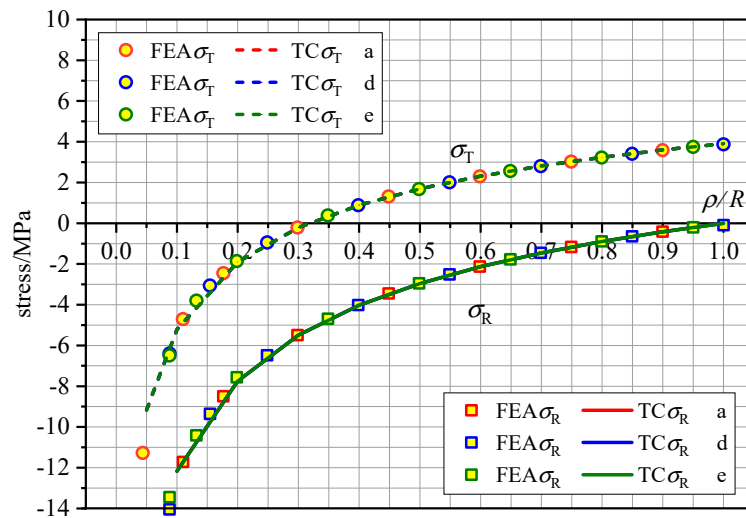


Figure 4. Results of finite element analysis.

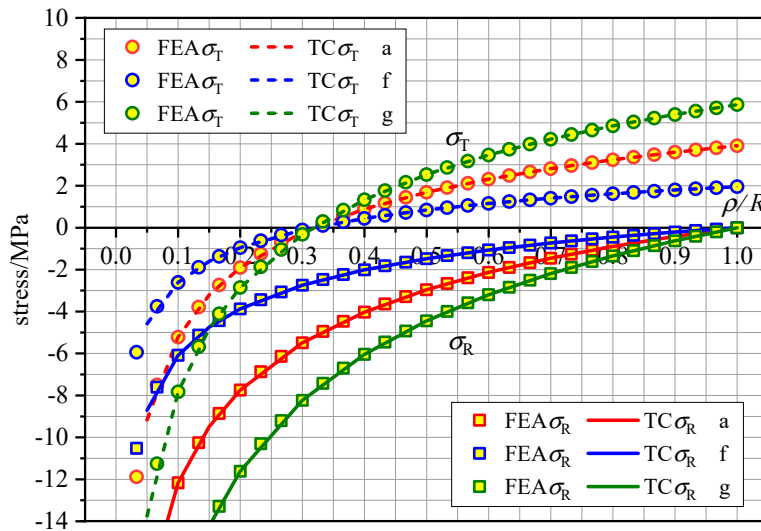


(a) Different  $W_i$  and  $W_e$  (same  $\Delta w$ )

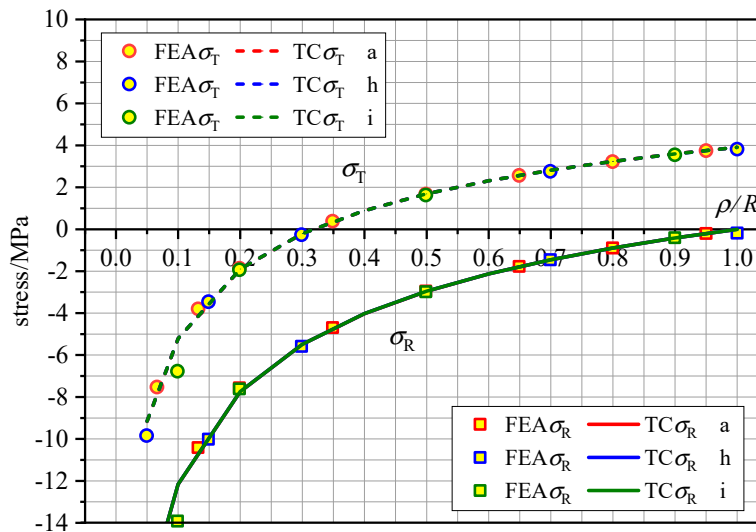
Figure 5. Cont.



(b) Different radii



(c) Different  $\Delta w$



(d) Different geometric shape

Figure 5. Comparison of finite element analysis and theoretical analysis.

The humidity stress distribution from the finite element analysis is shown in Figure 5, where the finite element analysis and theoretical calculation are designated FEA and TC, respectively. The proposed theoretical calculations of humidity stress distribution were highly consistent with the finite element analysis. Notably, the humidity stress expressions proposed in this research are reasonable and accurate.

Both radial stress and tangential stress curves were smooth. The radial stress is always compressive, whereas the tangential stress changes from compressive stress to tensile stress at the center of the circle. Therefore, tangential stress always has a critical point of tensile and compressive stress.

Furthermore, moisture stress is independent of initial moisture content  $W_i$ , equilibrium moisture content  $W_e$ , and member size but is related to the moisture content gradient  $\Delta w$ . Notably, if the cylinder cross-sectional transfer coefficient is 0, the stress distribution of the cylinder cross-section is the same as that of the disk under the same  $\Delta w$ . The three-dimensional cylindrical humidity stress distribution can be replaced by the two-dimensional disk for further calculations.

### 3. Prediction of Dry Shrinkage Crack Depth

#### 3.1. Basic Assumption

Basic assumption: the shrinkage deformation of the cracked part is assumed to be unconstrained, and the residual stress is ignored: it can be considered stress-free. The cracked part has no constraint in the deformation of the uncracked part, and the stress of the uncracked part is equivalent to the stress of a disk with a radius of  $\rho_c (=R - d_c)$ . When the difference in water content change does not exceed  $\Delta w_{cr}$  again, the crack is closed, and the stress of the uncracked part returns to the initial state (stress-free state). In contrast, when the difference in water content change exceeds  $\Delta w_{cr}$  again, it continues to expand, and the cumulative extended depth is equivalent to a one-time change in water cut.

To verify the validity of the above assumptions, the finite element simulation method is utilized. The verification involves (1) establishing a finite element model of presplit wood members; (2) setting a load condition for a specific moisture content change difference (greater than  $\Delta w_{cr}$ ); (3) extracting the stress distribution of wood members at any cracking position as cracking proceeds, especially the tangential stress at the critical position of the crack and the cracked position (cracking of the wood members will expand during calculation for the finite element model); and (4) comparing the critical position of the crack, the cracked position, and the tangential direction of the theoretical calculation model before cracking. Notably, if the tangential stress at the cracked position is much smaller than that at the critical position of the crack and the value obtained from the calculation results of the theoretical calculation model before cracking, and the critical position of the crack is close to that from the calculation results of the theoretical calculation model before cracking, the assumptions can be verified. The finite element model results were those obtained by the authors. The models are displayed in Table 5 and Figure 6.

**Table 5.** Basic parameters of the validation models.

Model	Geometric	Radius $R$	$n$	Crack Distribution	Preset Crack Depth	$\Delta w$
M1	Disc	$R = 50$ mm	1	-	10% of the radius (5 mm)	10%
M2	Disc	$R = 50$ mm	2	Equiangular distribution, $180^\circ$	10% of the radius (5 mm)	10%
M3	Disc	$R = 50$ mm	3	Equiangular distribution, $120^\circ$	10% of the radius (5 mm)	10%
M4	Disc	$R = 50$ mm	4	Equiangular distribution, $90^\circ$	10% of the radius (5 mm)	10%

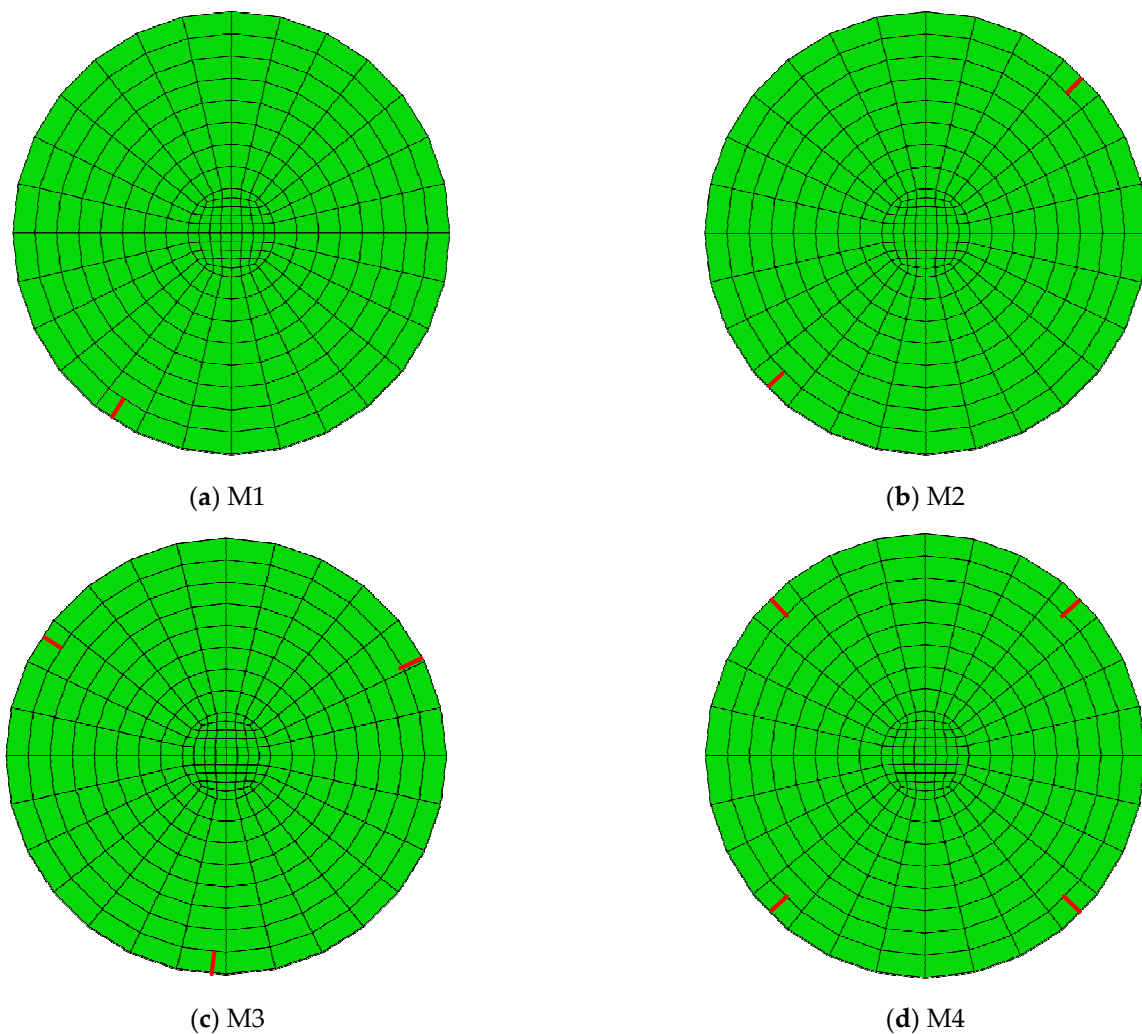


**Figure 6.** Finite element analysis model verified with basic assumptions.

The finite element calculation results of the above model are listed in Figure 7 and Table 6. Noticeably, the tangential stress at the cracked position is much smaller than that at the critical position of the crack and the values from the calculation results of the theoretical calculation model before cracking.

**Table 6.** Comparison of basic assumptions between the finite element model and the theoretical model.

Model- $d_c/R$	$\sigma_{R,c}$ (MPa)	$\sigma_{R,c_0-F}$ (MPa)	$\sigma_{R,c_0-T}$ (MPa)	$\frac{\sigma_{R,c_0-F}}{\sigma_{R,c_0-T}}$	Model- $d_c/R$	$\sigma_{R,c}$ (MPa)	$\sigma_{R,c_0-F}$ (MPa)	$\sigma_{R,c_0-T}$ (MPa)	$\frac{\sigma_{R,c_0-F}}{\sigma_{R,c_0-T}}$
M2-0.3	0.64	3.11	3.91	0.80	M4-0.3	0.27	3.26	3.91	0.83
M2-0.4	0.18	3.41	3.91	0.87	M4-0.4	1.01	3.23	3.91	0.83
M2-0.5	0.00	3.60	3.91	0.92	M4-0.5	1.05	3.06	3.91	0.78
M2-0.6	−0.05	3.63	3.91	0.93	M4-0.6	−0.03	3.01	3.91	0.77
M2-0.7	−0.07	3.20	3.91	0.82	M4-0.7	−0.05	2.99	3.91	0.76
Average of $\frac{\sigma_{R,c_0-F}}{\sigma_{R,c_0-T}}$ : 0.83									

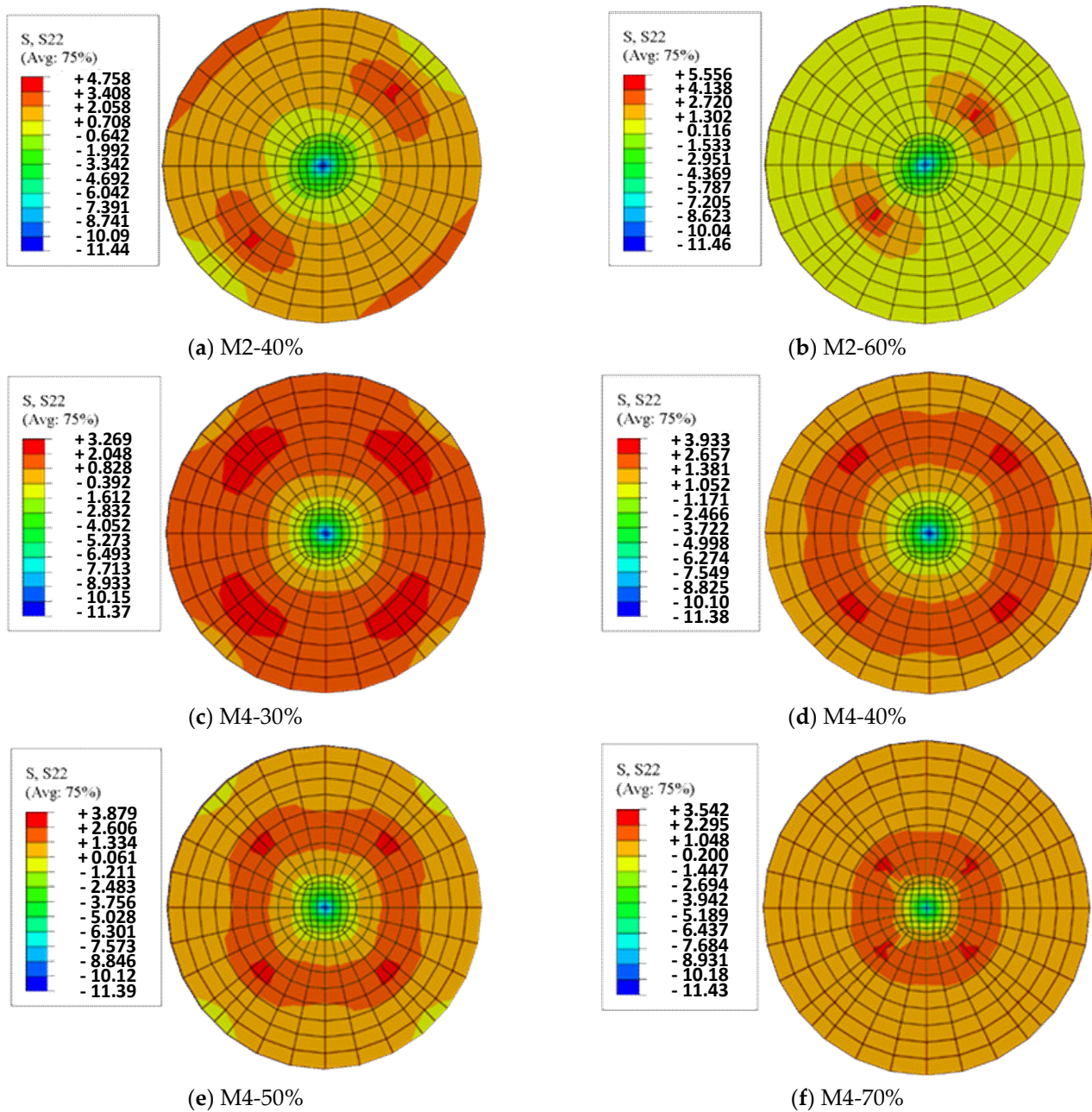


Figure 7. Finite element analysis results verified with basic assumptions.

### 3.2. Critical Moisture Content Gradient $\Delta w_{cr}$

When  $\sigma_T(\rho = R) = f_{t,T}$ , the periphery of the wood member is cracked, and the critical moisture content gradient  $\Delta w_{cr}$  can be obtained via Equations (23) and (24).

$$\sigma_T(\rho = R) = -\frac{K}{1 + \sqrt{\alpha_E}} = -\frac{E_T(\alpha_T - \alpha_R)\Delta w_{cr}}{1 + \sqrt{\alpha_E}} \quad (23)$$

$$\Delta w_{cr} = -\frac{(1 + \sqrt{\alpha_E})f_{t,T}}{E_T(\alpha_T - \alpha_R)} \quad (24)$$

According to Equation (22), the position at which the tangential stress is equal to zero  $\rho_0$  is unaffected by  $\Delta w$ . At the position  $\rho_0$ , the radial shrinkage deformation and the compression deformation are just equal to the circumferential shrinkage deformation. At  $r > \rho_0$ ,

tensile strain in the tangential direction is required to satisfy the coordinated displacement relationship. At the position  $r < \rho_0$ , the radial shrinkage deformation and the compression deformation exceed the circumferential shrinkage deformation, and circumferential compressive strain is required to meet the displacement coordination condition.

### 3.3. Dry Shrinkage Crack Depth

The stress distribution before and after cracking of the wood member based on the basic assumptions mentioned above is shown in Figure 8.

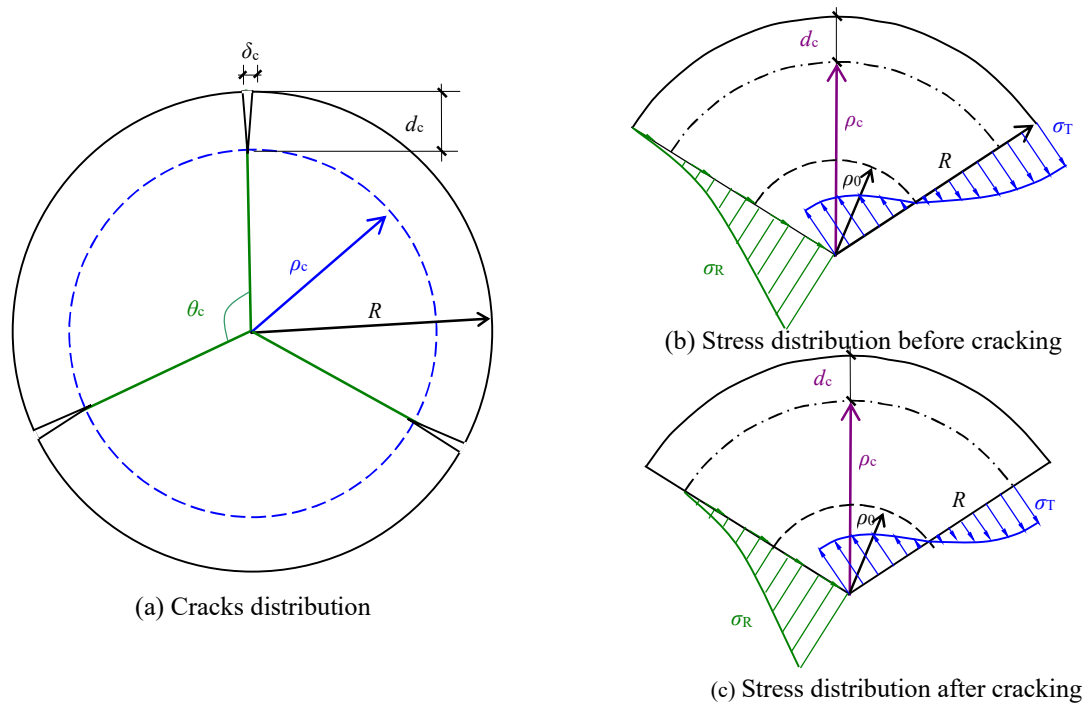


**Figure 8.** Stress distribution before and after cracking of wood components.

The hoop tensile stress at  $\rho_c$  is equal to  $f_T$ , as shown in Equations (25)–(27).

$$-\frac{E_T(\alpha_T - \alpha_R)\Delta w}{1 - \alpha_E} \left[ 1 - \sqrt{\alpha_E}(\rho_c/R)^{(\sqrt{\alpha_E}-1)} \right] = f_T = -\frac{E_T(\alpha_T - \alpha_R)\Delta w_{cr}}{1 + \sqrt{\alpha_E}} \quad (25)$$

$$\frac{\Delta w}{1 - \sqrt{\alpha_E}} \left[ 1 - \sqrt{\alpha_E}(\rho_c/R)^{(\sqrt{\alpha_E}-1)} \right] = \Delta w_{cr} \quad (26)$$

$$1 - \sqrt{\alpha_E}(\rho_c/R)^{(\sqrt{\alpha_E}-1)} = \frac{\Delta w_{cr}(1 - \sqrt{\alpha_E})}{\Delta w} \quad (27)$$

$\rho_c/R$  and  $d_c/R$  are, respectively, expressed by Equations (28) and (29).

$$\rho_c/R = \exp \left[ \frac{\ln \sqrt{\alpha_E} - \ln(1 - (1 - \sqrt{\alpha_E})\Delta w_{cr}/\Delta w)}{1 - \sqrt{\alpha_E}} \right] \quad (28)$$

$$d_c/R = 1 - \exp \left[ \frac{\ln \sqrt{\alpha_E} - \ln(1 - (1 - \sqrt{\alpha_E})\Delta w_{cr}/\Delta w)}{1 - \sqrt{\alpha_E}} \right] \quad (29)$$

The estimated calculated crack depth is shown in Figure 9.

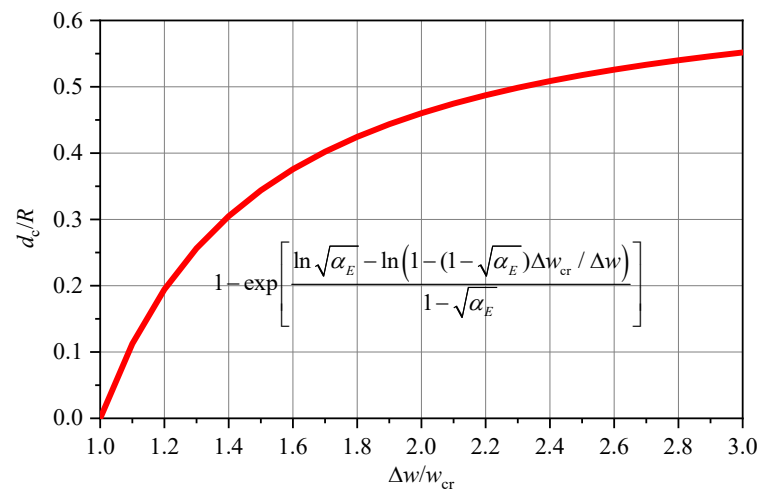


**Figure 9.** Relationship between  $d_c/R$  and  $\Delta w/\Delta w_{cr}$ .

#### 4. Validation

##### 4.1. Detection

The detected wood components were taken from old demolished residential houses located in Tianjin ( $117.2^\circ$  E,  $39.13^\circ$  N) and Liuzhou ( $109.42^\circ$  E,  $24.33^\circ$  N), China. These components were previously used as beams and columns, and their diameters ranged between 15 and 35 cm. These detected samples are from different environments, components, and tree species, mainly to verify the accuracy of crack depth prediction model (Equation (1)) through multiple parameters. The collectors recorded the relevant information of these wood components in detail, including the service life  $Y_d$ , tree species, use environment, component type, and rain conditions. It should be noted that all detected wood components are untreated wood. The detected wood components are presented in Figure 10.



(a) Tianjin 1



(b) Tianjin 2



(c) Liuzhou 1



(d) Cross-section—Tianjin



(e) Cross-section—Liuzhou

**Figure 10.** Wood components from practical engineering.

The detected parameters included the crack depth  $d_{c,i}$ , quantity of shrinkage cracks  $n$ , circumference of wood components  $c$ , and distance from the crack to the pith  $R_i$ . The average relative crack depth  $d_c/R$  is calculated from Equation (30). The basic parameters and detection results for the wood components are listed in Table 7.

$$\frac{d_c}{R} = \frac{\left(\frac{d_{c,1}}{R_1} + \frac{d_{c,2}}{R_2} + \dots + \frac{d_{c,n}}{R_n}\right)}{n} \quad (30)$$

**Table 7.** Necessary parameters and detected results of wood components.

Region	No.	Name	Species	$c$ (mm)	$n$	Rain Conditions	$Y_d$ (Year)	$d_c/R$ -E	$\Delta w_{cr}$ (%)	$\Delta w$ (%)	$d_c/R$ -T	Ratio (E/T)
Tianjin	1	TJ-Yu-42	Elm	552	4	✓, light	42	0.37	6.36	9.56	0.31	1.19
	2	TJ-Yu-60	Elm	540	5	✓, light	60	0.30	6.36	9.56	0.31	0.97
	3	TJ-Yang-60	Poplar	622	3	✓, light	60	0.40	5.90	9.56	0.38	1.05
	4	TJ-Liu-36	Willow	582	1	✓, light	36	0.24	7.30	9.56	0.23	1.06
	5	TJ-Song-52	Pine	514	7	✓, light	52	0.25	7.18	9.56	0.24	1.03
	6	TJ-Yu-52	Elm	647	4	✓, light	52	0.22	6.36	9.56	0.31	0.71
	7	TJ-Yang-42	Poplar	583	2	✓, light	42	0.49	5.90	9.56	0.38	1.29
	8	TJ-Yang-52	Poplar	563	4	✓, light	52	0.42	5.90	9.56	0.38	1.10
	9	TJ-Liu-60	Willow	608	1	✓, light	60	0.16	7.30	9.56	0.23	0.70
	10	TJ-Huai-36	Sophora	498	5	✓, light	36	0.22	7.20	9.56	0.20	1.12
	11	TJ-Yu-36	Elm	547	2	✓, light	36	0.40	6.36	9.56	0.31	1.29
	12	TJ-Huai-60	Sophora	616	10	✓, light	60	0.25	7.62	9.56	0.20	1.25
Liuzhou	13	LZ-Sha-70(a)	Spruce	962	4	x	70	0.44	6.10	9.13	0.37	1.19
	14	LZ-Sha-70(b)	Spruce	694	3	x	70	0.48	6.10	9.13	0.37	1.29
	15	LZ-Sha-60	Spruce	724	9	x	60	0.36	6.10	9.13	0.37	0.97
	16	LZ-Sha-55	Spruce	953	6	x	55	0.35	6.10	9.13	0.37	0.95
	17	LZ-Sha-50	Spruce	949	5	x	50	0.46	6.10	9.13	0.37	1.24
	18	LZ-Sha-45	Spruce	942	7	x	45	0.34	6.10	9.13	0.37	0.92
	19	LZ-Sha-40(a)	Spruce	725	6	x	40	0.37	6.10	9.13	0.37	1.00
	20	LZ-Sha-40(b)	Spruce	956	7	x	40	0.31	6.10	9.13	0.37	0.84
	21	LZ-Sha-30(a)	Spruce	704	5	x	30	0.39	6.10	9.13	0.37	1.05
	22	LZ-Sha-30(b)	Spruce	650	5	x	30	0.39	6.10	9.13	0.37	1.05
	23	LZ-Sha-30(c)	Spruce	659	5	x	30	0.33	6.10	9.13	0.37	0.89
	24	LZ-Sha-30(d)	Spruce	661	4	x	30	0.36	6.10	9.13	0.37	0.97
	25	LZ-Sha-30(e)	Spruce	629	5	x	30	0.44	6.10	9.13	0.37	1.19
	26	LZ-Sha-25	Spruce	602	6	x	25	0.36	6.10	9.13	0.37	0.97
	27	LZ-Sha-20	Spruce	617	6	x	20	0.39	6.10	9.13	0.37	1.05
	28	LZ-Sha-15	Spruce	645	7	x	15	0.34	6.10	9.13	0.37	0.92
	29	LZ-Sha-10	Spruce	617	5	x	10	0.45	6.10	9.13	0.37	1.22

Average ratio (E/T):1.051

Dispersion coefficient of Ratio (E/T): 15.10%

Note: If the relative crack depth  $d_c/R$  is less than 0.05, it is ignored. The lowercase letters (a) to (e) represent different samples of detected components with the same tree species and the same service life.

#### 4.2. Comparison

The calculation of the moisture content gradient  $\Delta w$  is based on the meteorological temperature ( $T$ ), humidity ( $RH$ ), and precipitation ( $pp$ ) in the external environment where these components were used. Bulcke [25] and Ladislav [26] provided a calculation method for moisture content that considers precipitation factors. This calculation method takes into account the impact of the rain period and the drying period on the moisture content of wood, with a rough linear relationship. Tianjin and Liuzhou have a temperate monsoon climate and subtropical monsoon climate, respectively. Furthermore, taking the 2017 data as an example, the meteorological data of the two regions are shown in Figure 11.

The wood components from Tianjin were placed in outdoor environment; thus, determining the moisture content necessitates considering rainwater factors. The annual water content gradient of Tianjin from 1951 to 2018 is based on the calculation method provided by Bulcke [25] and Ladislav [26]. The average moisture content gradient is then considered as  $\Delta w$ . In contrast, the wood components from Liuzhou were used in an indoor environment, so the moisture content can be calculated from Equation (31) [27]. Additionally, this paper uses the abovementioned method to calculate the annual moisture content gradient in Liuzhou from 1951 to 2018, and the average moisture content gradient is considered as  $\Delta w$ .

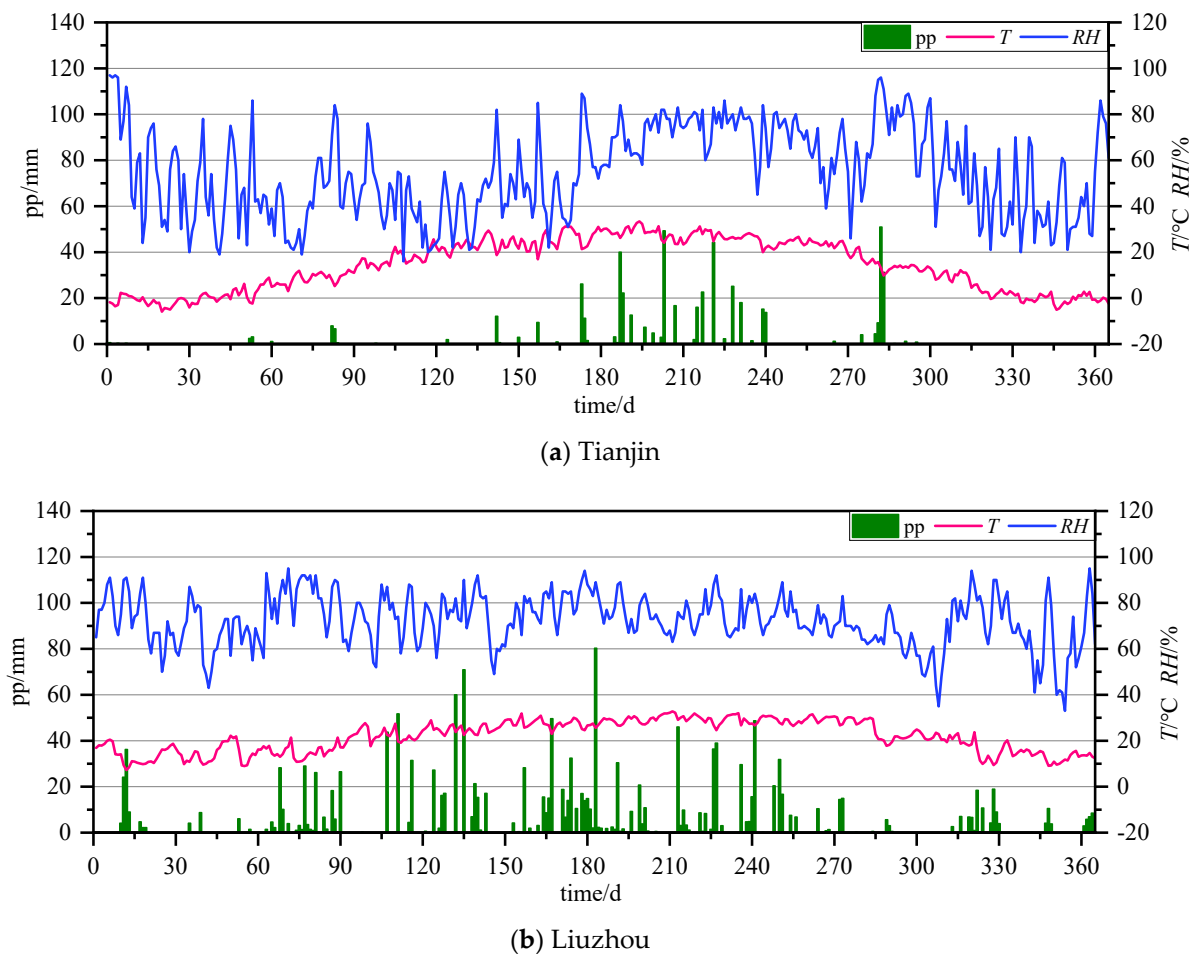


Figure 11. Meteorological data of Tianjin and Liuzhou (2017 as an example).

$$w = 0.01 \left[ \frac{-T \ln(1 - RH)}{0.13 \left(1 - \frac{T}{647.1}\right)^{-6.46}} \right]^{\frac{T^{0.75}}{110}} \quad (31)$$

where  $w$  represents moisture content;  $T$  and  $RH$  are the temperature and relative humidity, respectively.

The detection result of average relative crack depth  $d_c/R$ -E was compared with the calculation result  $d_c/R$ -T from Equation (29), and the comparison results are presented in Table 7 and Figure 12. The mechanical performance parameters of the wood materials considered were all sourced from the literature, books, and specifications [28–33]; in the absence of consistent data, the corresponding data of the approximate tree species were considered.

Figure 12 shows that the calculation results and the detection results are roughly similar, and most errors are within 30%. The errors are attributable to the following reasons: (1) The information is not completely accurate due to the age and variety of the detected wood components. Some detection components come from private demolished buildings, and these components have not been accurately recorded with sufficient information, only vague information. (2) The mechanical properties of wood materials are highly discrete. Some detection components only have one sample and approximate data are used in the calculation by references [28–33]. (3) The moisture content of the external environment involves an approximate calculation method, which cannot be completely accurate at present.

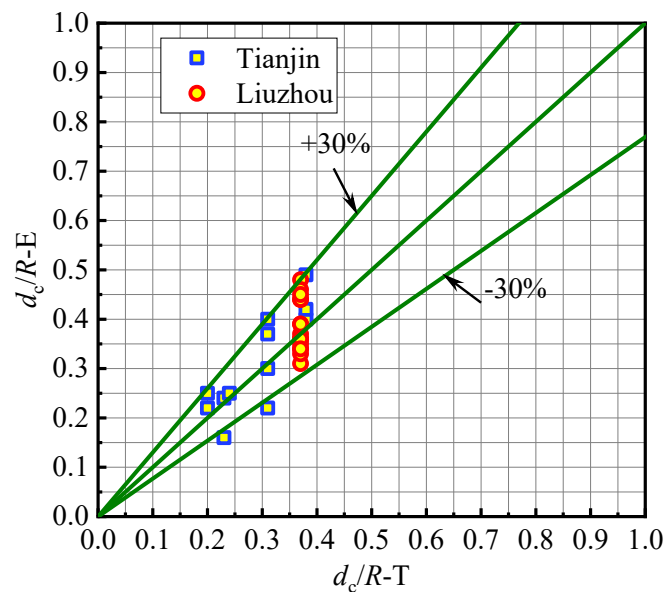


**Figure 12.** Comparison results of  $d_c/R-E$  and  $d_c/R-T$ .

In general, the predicted shrinkage crack depth model is feasible. First, the calculation of the humidity stress of wood components was verified via the finite element method. Second, the crack depth was inferred from the humidity stress distribution. Finally, the rationality of the crack depth calculation model was verified using old wooden components.

#### 4.3. Application of Prediction Model

Based on the above research results, the prediction model can be applied to practical wood engineering. Three steps are critical for application prediction model of practical wood engineering, as illustrated in Figure 13. Calculating the moisture content gradient  $\Delta w$  is the first step, and local meteorological data (temperature, humidity, and precipitation) needs to be collected before calculation. The second step is to calculate the critical moisture content gradient  $\Delta w_{cr}$ , which requires obtaining the wood parameters before. The final step is to predict the depth of the crack based on the calculation results of the first two steps.

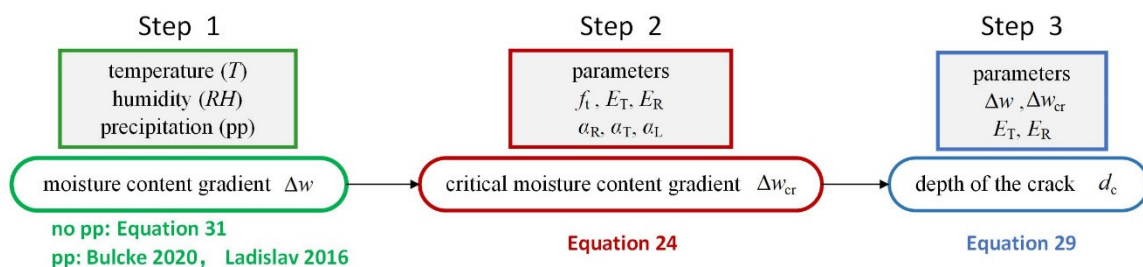


**Figure 13.** The application process of the formula to practical wood components [25,26].

## 5. Conclusions

This study highlights several important issues that are relevant to understanding the humidity stress distribution and shrinkage crack depth prediction model of timber components. The analytical solution of humidity stress was verified using finite element analysis. The shrinkage crack depth prediction model was validated using practical engineering detection data. The following are the main conclusions drawn:

- (1) The theoretical calculation of the humidity stress distribution proposed in this paper is in good agreement with the finite element results. Therefore, the expression of humidity stress is accurate and can provide a reliable basis for subsequent calculations.

- (2) The tangential stress of the disc is manifested as compressive stress at the center of the circle while tensile stress at the circumference. There is a continuous change from the center of the circle to the circumference, and a critical tension–compression point  $r$  exists. In contrast, the radial stress is always compressive from  $r = 0$  to  $r = 1$ .
- (3) The moisture stress is not determined by the initial moisture content  $W_i$ , equilibrium moisture content  $W_e$ , or member size but by the difference in moisture content  $\Delta w$ .
- (4) The distribution of humidity stress in the cross-section of a three-dimensional cylinder is consistent with that of a two-dimensional disk under the same conditions. Furthermore, the three-dimensional cylindrical humidity stress distribution can be simplified as a two-dimensional disk for further calculation.
- (5) An approximate shrinkage crack depth prediction model based on reasonable humidity stress expressions was proposed. Although this has scope for engineering application development, several issues that must first be clarified in detail persist, including approximately similar maximum tensile stress and wood tensile strength and the fact that the crack tip stress and residual stress were ignored.
- (6) The abovementioned shrinkage crack prediction model was verified via practical engineering testing. The test data are in good agreement with the theoretical calculation data of the model. The above model can be applied to actual engineering prediction to provide a theoretical basis for the reinforcement measures and the safety evaluation of wood structures.
- (7) The proposed three-step application process provide a basis on the prediction of shrinkage crack in practical wood engineering for further research.

**Author Contributions:** P.T.: Investigation, Experiment, Data curation, Original draft preparation, Software, Validation, Writing—Reviewing and Editing. H.Q.: Conceptualization, Methodology, Validation, Supervision. J.H.: Data curation, Original draft preparation. H.L.: Investigation, Writing—Reviewing and Editing. X.H.: Methodology, Supervision, Investigation. All authors have read and agreed to the published version of the manuscript.

**Funding:** This study was sponsored by the Natural Science Foundation of Xinjiang Uygur Autonomous Region (2022D01C687).

**Data Availability Statement:** The data is unavailable due to privacy or ethical restrictions.

**Acknowledgments:** The authors would like to express their gratitude to Key Laboratory of Concrete and Prestressed Concrete Structure of Ministry of Education, Southeast University.

**Conflicts of Interest:** The authors declare no conflict of interest.

## Nomenclature

$\Delta w$	Moisture content gradient
$w_{\max}$	Maximum moisture content
$w_{\min}$	Minimum moisture content
R, T, L	Radial direction, tangential direction, longitudinal direction of wood
$f_t$	Tensile strength in cross-section
$f_{t,R}, f_{t,T}, f_{t,L}$	Radial/tangential/longitudinal tensile strength in cross-section
$f_c$	Compressive strength in cross-section
$f_{c,R}, f_{c,T}, f_{c,L}$	Radial/tangential/longitudinal compressive strength in cross-section
$\alpha_R, \alpha_T, \alpha_L$	Radial/tangential/longitudinal shrinkage and swelling coefficient
R, L	Radius/length of the disc
$\delta_R, \delta_T$	Radial/tangential deformation difference
$\delta_{R,sh}, \delta_{T,sh}$	Radial/tangential deformation difference caused by shrinkage
$\delta_{R,F}, \delta_{T,F}$	Radial/tangential deformation difference caused by force
$\theta$	Any angle of the disc
$\sigma_R, \sigma_T$	Radial/tangential humidity stress
$\rho/R$	Relative distance from the center of the circle
$\rho_0/R$	Critical relative distance
$E_R, E_T, E_L$	Radial/tangential/longitudinal elastic modulus

$\varepsilon_R, \varepsilon_T$	Radial/tangential strain
$\nu_{RT}, \nu_{RL}, \nu_{TL}$	Poisson's ratio of different directions
$G_{RT}, G_{RL}, G_{TL}$	Shear modulus of different directions
$d_c$	Depth of the crack
$\rho_c/R$	Relative distance from the center of the circle after cracking
$\Delta w_{cr}$	Critical moisture content gradient
$Y_d$	The service life of wood components have been used for
$c$	Circumference of wood components
$n$	Number of cracks in wood components
$d_c/R$	Relative crack depth of wood components in cross-section

## References

- Kang, W.; Lee, N.-H.; Choi, J.-H. A radial distribution of moistures and tangential strains within a larch log cross section during radio-frequency/vacuum drying. *Holz Als Roh-Und Werkst.* **2004**, *62*, 59–63. [\[CrossRef\]](#)
- Svensson, S.; Toratti, T. Mechanical response of wood perpendicular to grain when subjected to changes of humidity. *Wood Sci. Technol.* **2002**, *36*, 145–156. [\[CrossRef\]](#)
- Jönsson, J. *Moisture Induced Stresses in Glulam Cross Sections*; CIB-W18/34-12-4; Konferenzbeitrag: Venice, Italy, 2001.
- Jönsson, J.; Svensson, S. A contact free measurement method to determine internal stress states in glulam. *Holzforschung* **2004**, *58*, 148–153. [\[CrossRef\]](#)
- Jönsson, J. Internal stresses in the cross-grain direction in glulam induced by climate variations. *Holzforschung* **2004**, *58*, 154–159. [\[CrossRef\]](#)
- Gereke, T. *Moisture-Induced Stresses in Cross-Laminated Wood Panels*. Ph.D. Thesis, ETH Zurich, Zurich, Switzerland, 2009.
- Fragiacomo, M.; Fortino, S.; Taroni, D.; Usardi, I.; Toratti, T. Moisture-induced stresses perpendicular to grain in cross-sections of timber members exposed to different climates. *Eng. Struct.* **2011**, *33*, 3071–3078. [\[CrossRef\]](#)
- Morihiko, T. Casehardening and drying set in the kiln-drying of wood III, Changes of set in slices from the outside to the center of wood pieces during conditioning. *Mokuaai Gakkaishi* **1989**, *3*, 300–392.
- Mohager, S.; Toratti, T. Long term bending creep of wood in cyclic relative humidity. *Wood Sci. Technol.* **1992**, *27*, 49–59. [\[CrossRef\]](#)
- Cheng, X.; Li, X.; Huang, Q.; Sun, H.; Li, Y.; Xie, J.; Xiong, X. The study of moisture content and inner stress variation of kiln-dried wood during equalization treatment. *J. For. Eng.* **2016**, *1*, 38–43.
- Gao, X. *Fatigue of Wood Subjected to Cyclic Moisture-induced Stress Perpendicular to Grain*. Master's Thesis, Harbin Institute of Technology University, Harbin, China, 2016.
- Arends, T.; Pel, L.; Huinink, H.P. Hygromorphic response dynamics of oak: Towards accelerated material characterization. *Mater. Struct.* **2017**, *50*, 181. [\[CrossRef\]](#)
- Liu, J.; Wang, X. Effect of Drying Temperature and Relative Humidity on Contraction Stress in Wood. *BioResources* **2016**, *11*, 6625–6638. [\[CrossRef\]](#)
- Wang, H.H.; Youngs, R.L. Drying stress and check development in the wood of two oaks. *IAWA J.* **1996**, *17*, 15–30. [\[CrossRef\]](#)
- Kawa, S. Computation of drying stresses resulting from moisture gradients in wood during. I. Computative method. *Mokuaai Gakkaishi* **1979**, *2*, 103–110.
- Chen, X.; Zhu, E. Moisture and Thermal Stress in Glulam Beams. *Ind. Constr.* **2008**, *z1*, 862–866.
- Gereke, T.; Niemz, P. Moisture-induced stresses in spruce cross-laminates. *Eng. Struct.* **2010**, *32*, 600–606. [\[CrossRef\]](#)
- Angst, V.; Malo, K.A. Moisture-induced stresses in glulam cross sections during wetting exposures. *Wood Sci. Technol.* **2013**, *47*, 227–241. [\[CrossRef\]](#)
- Arends, T.; Barakat, A.J.; Pel, L. Moisture transport in pine wood during one-sided heating studied by NMR. *Exp. Therm. Fluid Sci.* **2018**, *99*, 259–271. [\[CrossRef\]](#)
- Zhao, J. *Research on Drying Characteristics and Check within White Birch Disks*. Ph.D. Thesis, Northeast Forestry University, Harbin, China, 2013.
- Fan, C.; Wang, L.; Pan, J. Measures to control seasoning checks of wood used for the repair of the ancient wooden towers in Yingxian County, Shanxi Province. *J. Beijing For. Univ.* **2006**, *1*, 98–102.
- Wang, X. *Research on Evaluation Method of Reliability-Based Residual Life of Historic Timber Structures*. Ph.D. Thesis, Wuhan University of Technology, Wuhan, China, 2008.
- Angellier, N.; Pitti, R.M.; Dubois, F. *Crack Analysis of Wood under Climate Variations*; Springer: Berlin/Heidelberg, Germany, 2016; pp. 235–242.
- Chen, K.; Qiu, H.; Sun, M.; Lam, F. Experimental and numerical study of moisture distribution and shrinkage crack propagation in cross section of timber members. *Constr. Build. Mater.* **2019**, *221*, 219–231. [\[CrossRef\]](#)
- Brischke, C.; Selzer, V. Mapping the Decay Hazard of Wooden Structures in Topographically Divergent Regions. *Forests* **2020**, *11*, 510. [\[CrossRef\]](#)
- Reinprecht, L. *Wood Deterioration, Protection and Maintenance*; John Wiley & Sons, Ltd.: London, UK, 2016; pp. 126–142.
- Hanhijarvi, A.O. *Modelling of Creep Deformation Mechanism in Wood*; Espoo 15; Technical Research Cent of Finland: Espoo, Finland, 1995; p. 231.

28. Xu, B.H.; Bouchaïr, A.; Racher, P. Appropriate Wood Constitutive Law for Simulation of Nonlinear Behavior of Timber Joints. *J. Mater. Civ. Eng.* **2014**, *26*, 04014004-1. [[CrossRef](#)]
29. Xu, B.H.; Bouchaïr, A.; Taazount, M.; Vega, E.J. Numerical and experimental analyses of multiple-dowel steel-to-timber joints in tension perpendicular to grain. *Eng. Struct.* **2009**, *31*, 235–236. [[CrossRef](#)]
30. Larsen, F.; Ormarsson, S. Numerical and experimental study of moisture-induced stress and strain field developments in timber logs. *Wood Sci. Technol.* **2013**, *47*, 837–852. [[CrossRef](#)]
31. Zhou, H. Experimental and Analysis of the Mechanical Behavior of Bolted Joints with Slotted-in Steel Plate in Timber Structures. Master's Thesis, Harbin Institute of Technology University, Harbin, China, 2017.
32. He, Z. The Experimental Study on Mechanical Property of Bolted Joint with Glued Timber and Steel Plate. Master's Thesis, Central South University of Forestry and Technology, Changsha, China, 2017.
33. Zhao, Y.; He, M.; Ma, R. Bending bearing capacity and parametric analysis of prestressed tube bolted timber connections. *J. Build. Struct.* **2016**, *37*, 18–26.

**Disclaimer/Publisher's Note:** The statements, opinions and data contained in all publications are solely those of the individual author(s) and contributor(s) and not of MDPI and/or the editor(s). MDPI and/or the editor(s) disclaim responsibility for any injury to people or property resulting from any ideas, methods, instructions or products referred to in the content.